Materials Science in Semiconductor Processing 103 (2019) 104620

Contents lists available at ScienceDirect

Materials Science in Semiconductor Processing

journal homepage: www.elsevier.com/locate/mssp

Temperature dependent current-voltage characteristics of Al/TiO_2/*n*-Si and Al/Cu:TiO_2/*n*-Si devices

Mehmet Okan Erdal[a], Adem Kocyigit[b], Murat Yıldırım[c,*]

[a] Necmettin Erbakan University, Meram Vocational School, 42090, Konya, Turkey
[b] Igdir University, Engineering Faculty, Department of Electrical Electronic Engineering, 76000, Igdir, Turkey
[c] Selcuk University, Faculty of Science, Department of Biotechnology, 42130, Konya, Turkey

ARTICLE INFO

Keywords:
Cu doped TiO_2 thin films
Al/TiO_2/*n*-Si
Temperature-dependent *I–V* characteristics
Spin coating

ABSTRACT

We fabricated undoped and Cu doped TiO_2 thin films by spin coating technique and employed the films as interfacial oxide layer between the Al and *n*-type Si to investigate the effect of temperature on the Al/TiO_2/*n*-Si and Al/Cu:TiO_2/*n*-Si devices. For that aim, the *I–V* measurements were performed in the range of 50 K–400 K by 50 K interval. The devices exhibited good rectifying behavior and thermal response in a wide range temperature. Ideality factor, barrier height and series resistance were calculated from *I–V* measurements for various temperatures by thermionic emission theory, Norde and Cheung methods and discussed in the details. The obtained results revealed that the device parameters are a strong function of the temperature. The interface states (N_{ss}) were affected by the changing of the temperatures. The Al/TiO_2/*n*-Si and Al/Cu:TiO_2/*n*-Si devices can be performed for wide range temperatures in various technological applications.

1. Introduction

The metal oxides have great interest due to their adjustable behaviors such as band gap, mobility and conductivity [1–5]. These properties provide good opportunity to employ them for various applications such as solar cells, lasers, photodetectors and photodiodes [6–10]. Among the metal oxide family, TiO_2 has high dielectric constant, high refractive index and good optical transmittance in the visible range [11,12]. The high dielectric constant in the range of 35–100 makes it a good candidate to be an interlayer for metal-semiconductor devices (MS) both to prevent inter-diffusion and to passivate interface states and dislocations [13]. Thus, the performance of the MS devices can be improved by that way.

The MS devices have gained great attention because of their variety of applications such as inverters, rectifiers and photodiodes [14–16]. The device properties of the MS can be controlled by the interfacial layers via metal oxide or insulators [17–19]. Especially, the TiO_2 film layers were employed as the interfacial layer in the literature. For example, Asar et al. [13] investigated voltage and temperature dependent dielectric properties of the (AuZn)/TiO_2/*p*-GaAs MIS device which had TiO_2 interlayer in the temperature range of 80 K–290 K. Tanrıkulu et al. [20] obtained Au/TiO_2/*n*-4H–SiC MS device with TiO_2 interlayer and investigated its main electrical and dielectric properties via impedance spectroscopy. They concluded that the TiO_2 interlayer improved the performance of the MS device. Bilgili et al. [21] fabricated Ag/TiO_2/*n*-InP MS device and performed the *I–V* measurements on the device for wide range temperatures from 120 K to 420 K. Tataroğlu et al. [22] studied NiO-doped TiO_2 film in between *n*-Si and Al metal as interfacial layer and concluded that the obtained device exhibited good photoconductivity and photoresponsivity via changing NiO contents. Yıldırım [23] investigated both optical and electrical properties of the various Cu doped TiO_2 interfacial layer between the Al and *n*-Si at room temperature. The photoresponse behavior of TiO_2 is greatly influenced by its crystal structure, particle/grain size, crystallinity, surface area, and porosity. Furthermore, various techniques have been employed to enhance its properties by doping with metal or non-metal elements in order to narrow its band gap [24]. The modification of Cu dopant can be improved the photoresponse and photocurrent density of TiO_2. Moreover, Cu dopants have already shown to play an important role in the effective charge separation in TiO_2 electron harvesting processes [25]. Blondeau et al. claim that applications for solar energy conversion of doping TiO_2 with an element taken from metals, their results have shown that this alloying has created an extra level of absorption at energy within the bandgap of TiO_2. They have also shown that the concentration of this foreign element was very important to obtain a practical result [26].

In this case, we studied the temperature dependent *I–V* characteristics of the Cu doped TiO_2 interfacial layer. It is therefore, we studied

* Corresponding author.
E-mail address: muratyildirim@selcuk.edu.tr (M. Yıldırım).

https://doi.org/10.1016/j.mssp.2019.104620
Received 11 April 2019; Received in revised form 4 June 2019; Accepted 13 July 2019
Available online 17 July 2019

undoped and Cu doped TiO_2 thin films between the metal and semiconductor as interfacial layer by *I–V* measurement in wide range temperatures from 50 K to 400 K and compared Al/TiO_2/*n*-Si and Al/Cu:TiO_2/*n*-Si devices according to various device parameters.

2. Materials and methods

Undoped and Cu doped TiO_2 thin films were obtained by precursors titanium (IV) isopropoxide ($Ti[OCH(CH_3)_2]_4$) and host copper nitrate ($Cu(NO3)_2{\cdot}3H_2O$). Firstly, the titanium (IV) isopropoxide was dissolved in the alcohol and acetylacetone mixture (35:1). In a different vessel, the copper (II) nitrate was solved in 10 mL alcohol. The titanium (IV) isopropoxide solution was used for synthesizing undoped TiO_2 thin film. The Cu doped TiO_2 thin film was obtained by the mixture of the two solutions, and the mixture was stirred for 30 min 2 mL glacial CH_3CO_2H, 2 mL deionized water and 20 mL alcohol were added to the mixed solution and stirred again 5 h. This mixture was employed to synthesize Cu doped TiO_2 thin film.

The *n*-type Si wafer was used as a substrate and semiconductor. The wafer had (100) preferred crystalline orientation and 7.5×10^{16} cm^{-3} carrier concentration. The *n*-type Si wafer was cut to 2 cm^2 pieces, and then the pieces were cleaned by acetone and isopropanol alcohol in an ultrasonic bath and dried in nitrogen. The pieces were dumped into HF:H_2O (1:1) mixed solution to remove the impurities and native SiO_2 oxide layers from the surfaces. To obtain ohmic contact on the back surface of the Si pieces, highly pure Al (99.999%) was evaporated at 150 nm thicknesses at 5×10^{-6} torr pressure. The Si wafer pieces were annealed in nitrogen medium at 500 °C for 3 min after Al evaporation. The obtained solutions for undoped and Cu doped TiO_2 thin films were deposited on the front surface of *n*-Si substrates by spin coating technique at 1200 rpm spin speed in 60 s spinning time with Fytronix SC-500 spin coater. The another Al layer was evaporated thermally on the undoped and Cu doped TiO_2 thin films via hole array mask. The hole radius was determined as 7.85×10^{-3} cm^2. The schematic diagram of the obtained Al/TiO_2/*n*-Si and Al/Cu:TiO_2/*n*-Si devices has been displayed in Fig. 1. The undoped and Cu doped TiO_2 thin films are hole transport layer, and there are ohmic contact between the Si and TiO_2 layers. However, the resistance between the TiO_2 and Si is high. Thus, undoped and Cu doped TiO_2 interfacial layer can be considered for controlling of the current transport mechanism.

The thicknesses of the obtained undoped and Cu doped thin films were measured by stylus profilometre (Veeco Dektak). The thickness information of the layers of two devices and doped amount of Cu are given in detail in our previous study [23]. Fytronix FY-7000 Electronic Device characterization system was employed for the *I–V* measurements of the devices by using a cryostat and temperature controller system. The measurement temperatures were changed in the range of 50–400 K by 50 K steps.

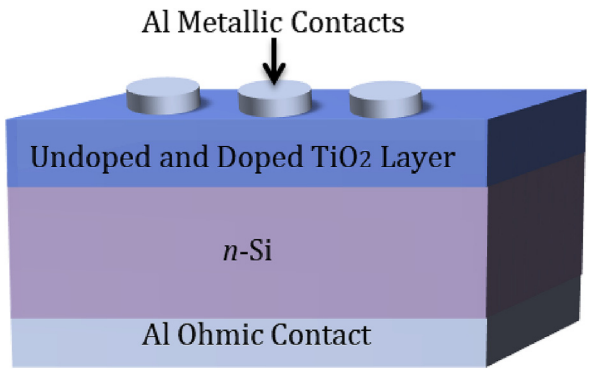

Fig. 1. Schematic diagram of the Al/TiO_2/*n*-Si and Al/Cu:TiO_2/*n*-Si devices.

3. Result and discussion

Fig. 2a and b exhibit the *I–V* characteristics of the Al/TiO_2/*n*-Si and Al/Cu:TiO_2/*n*-Si devices for various temperatures in the range of 50 K–400 K. Both devices displayed good rectifying properties for all temperatures, and calculated rectifying ratio (*RR*) values of the Al/TiO_2/*n*-Si and Al/Cu:TiO_2/*n*-Si devices were tabulated in Table 1 and Table 2. The determined *RR* values imply that the obtained device can be employed in a wide range temperature as rectifier [27,28]. The *RR* values decreased with increasing temperature for both devices. The decrease at the *RR* values via increasing temperature can be attributed to increasing reverse current flow [29]. In addition, the rectifying properties of the Al/TiO_2/*n*-Si device decreased with Cu doping depending on increasing carriers in the interface of the device. More carriers in the interface increase the current flow at reverse biases and decrease the *RR* value of the device. Furthermore, the current values of the devices increased with increasing temperature, and so the devices can be used as a thermal detector at reverse biases [30]. Moreover, the doping of the TiO_2 with Cu caused to increase the current at forward biases by increasing temperature (Fig. 2b).

To obtain device parameters such as barrier height and ideality factor, thermionic emission theory can be performed on the *I–V* measurements. According to this theory, the current (*I*) is given via the following formula:

$$I = I_0 \exp\left(\frac{qV}{nkT}\right)\left[1 - \exp\left(-\frac{qV}{nkT}\right)\right] \tag{1}$$

where I_0 is saturation current and determined the intercept value of the linear portion of ln*I*-*V* plot at zero voltage. The q, *n*, k and *T* represent charge of the electron, ideality factor, Boltzman's constant and temperature, respectively. The I_0 is given by following equations according to thermionic emission theory:

$$I_0 = AA^*T^2 \exp\left(-\frac{q\Phi_b}{kT}\right) \tag{2}$$

where Φ_b shows the barrier height at zero bias, *A* and A^* are contact area of the device and Richardson constant ($A^* = 112$ $Acm^{-2}K^{-2}$ for *n*-type Si), respectively. If equations (1) and (2) are rearranged, the *n* and Φ_b are obtained by next formulas:

$$n = \frac{q}{kT}\left(\frac{dV}{dlnI}\right) \tag{3}$$

and

$$\Phi_b = \frac{kT}{q} ln\left(\frac{A^*AT^2}{I_0}\right) \tag{4}$$

The *n* and Φ_b values were calculated for the Al/TiO_2/*n*-Si and Al/Cu:TiO_2/*n*-Si devices by equations of (3) and (4), and tabulated in Tables 1 and 2. Furthermore, Fig. 3a and b shows the temperature dependent profile of the *n* and Φ_b values of the Al/TiO_2/*n*-Si and Al/Cu:TiO_2/*n*-Si devices, respectively. While the Φ_b values of the Al/TiO_2/*n*-Si and Al/Cu:TiO_2/*n*-Si devices almost linearly increased with increasing temperature, the *n* values decreased exponentially. On the other hand, the *n* values increased after room temperature for the Al/TiO_2/*n*-Si device. Normally, both *n* and Φ_b values are not affected by the change of the temperature for Schottky devices. The temperature dependence at the *n* and Φ_b values can be attributed to that the devices have not pure thermionic emission transport mechanism [31]. The deviation from the thermionic emission mechanism can be depended on the barrier inhomogeneities due to the no*n*-uniform interfacial TiO_2 layers, its thickness and non-uniform charge distribution between the Al and *n*-Si [31,32]. Although the devices have high barrier height, flowing of the charge carriers is provided by lower parts of barrier height [33]. This means that the barrier height is not homogeneous, and the device exhibits unstable barrier height and ideality factor values

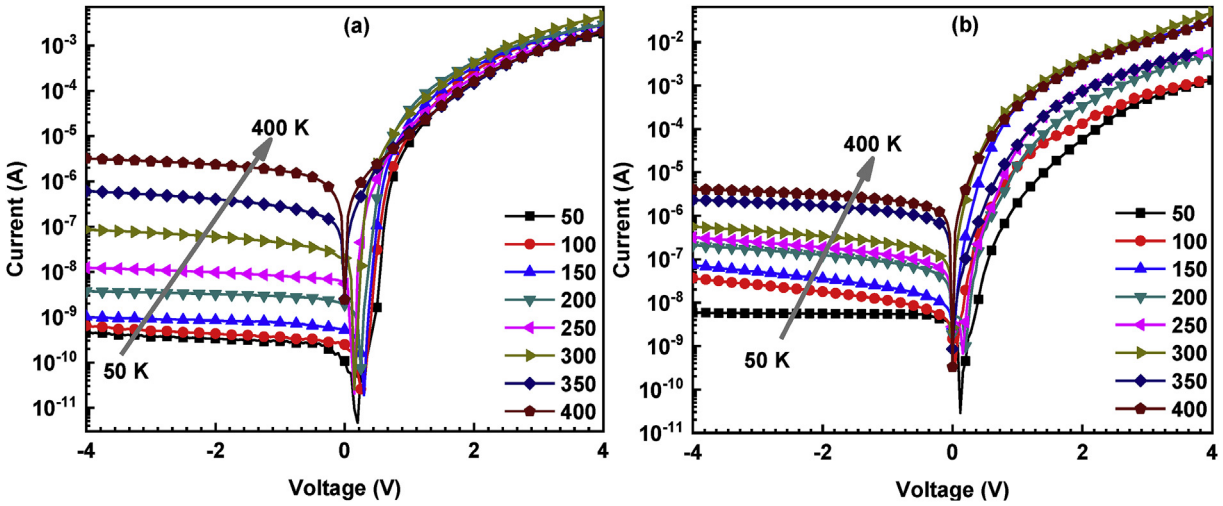

Fig. 2. Ln*I-V* plots of the a) Al/TiO_2/*n*-Si and b) Al/Cu:TiO_2/*n*-Si for various temperature.

Table 1
The obtained device parameters of the Al/TiO_2/*n*-Si device for the various methods.

T(K)	I_o Saturation Current	n (TE)	n (Cheung)	Φ_b(TE)	Φ_b(Cheung)	Φ_b(Norde)	R_s (Cheung) (dv/dlnI-I) (kΩ)	R_s (Cheung) (H(I)–I) (kΩ)	R_s (Norde) (F(V)–V) (kΩ)	RR
50	1.47×10^{-13}	21.9	24.1	0.16	0.12	0.15	14.1	14.3	3.89	2.01×10^{6}
100	2.78×10^{-13}	10.4	11.4	0.33	0.25	0.31	12.4	11.3	2.52	2.56×10^{6}
150	3.83×10^{-13}	6.18	6.59	0.50	0.39	0.49	11.5	11.0	2.24	1.42×10^{6}
200	6.83×10^{-12}	4.33	4.56	0.62	0.53	0.65	6.11	4.65	1.83	3.95×10^{5}
250	2.06×10^{-11}	2.91	3.18	0.77	0.70	0.77	36.8	22.0	6.36	7.85×10^{4}
300	1.83×10^{-11}	1.93	2.26	0.93	0.84	0.98	35.6	18.1	3.27	2.49×10^{4}
350	1.63×10^{-8}	5.66	5.44	0.89	0.83	0.88	25.4	21.3	8.21	1.52×10^{3}
400	1.09×10^{-7}	8.02	8.28	0.96	0.91	0.93	11.9	9.32	9.42	2.70×10^{2}

$\Delta n = 0.43$ and $\Delta\Phi_b = 0.0825$ eV (average absolute errors).

Table 2
The determined device parameters of the Al/Cu:TiO_2/*n*-Si for the various methods.

T(K)	I_o Saturation Current	n (TE)	n (Cheung)	Φ_b(TE)	Φ_b(Cheung)	Φ_b(Norde)	R_s (Cheung) (dv/dlnI-I) (kΩ)	R_s (Cheung) (H(I)–I) (kΩ)	R_s (Norde) (F(V)–V (kΩ)	RR
50	3.07×10^{-11}	35.8	50.8	0.14	0.11	0.13	3.06	3.08	1.15	8.68×10^{4}
100	1.02×10^{-9}	16.8	19.6	0.26	0.22	0.24	5.64	5.87	4.43	2.45×10^{4}
150	1.02×10^{-8}	11.0	7.62	0.37	0.34	0.35	0.96	0.76	0.18	2.19×10^{5}
200	2.07×10^{-10}	7.94	8.81	0.57	0.48	0.55	2.13	2.15	1.25	1.09×10^{4}
250	1.72×10^{-10}	6.25	7.53	0.72	0.59	0.71	0.97	0.88	0.76	1.11×10^{4}
300	9.02×10^{-8}	5.19	5.56	0.71	0.64	0.69	0.42	0.41	0.38	3.10×10^{4}
350	5.77×10^{-9}	5.10	5.93	0.92	0.82	0.92	0.90	0.77	1.76	1.40×10^{3}
400	3.48×10^{-7}	5.18	4.82	0.92	0.86	0.91	0.58	0.51	0.34	2.76×10^{3}

$\Delta n = 3.73$ and $\Delta\Phi_b = 0.0687$ eV (average absolute errors).

depending on temperature [34–36]. The barrier inhomogenities can be controlled by uniform and wonderful interfacial layers [37].

All the ideality factor values of the Al/TiO_2/*n*-Si and Al/Cu:TiO_2/*n*-Si devices at various temperatures are bigger than one. These higher ideality factor values also can be attributed to interface states and barrier inhomogeneity depending on the interfacial layer of undoped and Cu doped TiO_2 thin film [38,39]. Furthermore, the saturation current values, which are shown in Tables 1 and 2, of the Al/TiO_2/*n*-Si and Al/Cu:TiO_2/*n*-Si devices increased with increasing temperature, but Al/Cu:TiO_2/*n*-Si device has higher saturation current value than the Al/TiO_2/*n*-Si device.

Fig. 4a and b displays the *nkT* versus *kT* plot of the Al/TiO_2/*n*-Si and Al/Cu:TiO_2/*n*-Si devices, respectively. *nkT-kT* plots provide to better understand of the current mechanism for these kinds of devices. In the case of the ideal Schottky device, pure thermionic emission transport mechanism is an effective mechanism [36]. In the pure thermionic emission condition, the barrier height and ideality factor values are not functions of the temperature, and *nkT-kT* graphs exhibit a linear plot with unity slope. In our study, the devices are not ideal Schottky device and showed thermionic field emission behavior associated with thermionic emission current transport mechanism. This results confirmed also the barrier inhomogeneity of the devices [40].

The Richardson or the $\ln(I_0/T^2)$ versus $(kT)^{-1}$ - $(nkT)^{-1}$ plots of the Al/TiO_2/*n*-Si and Al/Cu:TiO_2/*n*-Si devices have been indicated in Fig. 5a and b, respectively. Normally, the Richardson constant of the *n*-type Si is 112 A/$(cmK)^{-1}$, but we obtained 3.53×10^{-6} and 1.11 A/$(cmK)^{-1}$ for the Al/TiO_2/*n*-Si and Al/Cu:TiO_2/*n*-Si devices as lower Richardson constant than 112 A/$(cmK)^{-1}$. This case confirms the barrier inhomogeneity at the interface of the devices [36]. The Richardson constant of the Al/Cu:TiO_2/*n*-Si device is so higher than that of the Al/TiO_2/*n*-Si device. This difference may be attributed to increasing charge carriers via Cu doping of TiO_2.

The Cheung method can be employed to determine the device parameters as well as series resistance (R_s) of the devices. When the R_s

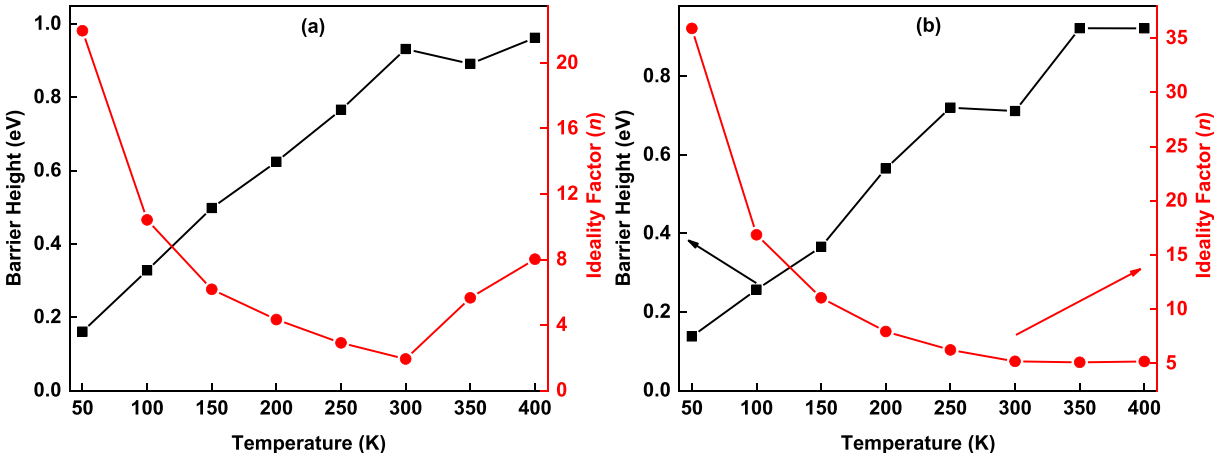

Fig. 3. Temperature dependent profile of the n and Φ_b values of the a) Al/TiO_2/n-Si and b) Al/Cu:TiO_2/n-Si devices.

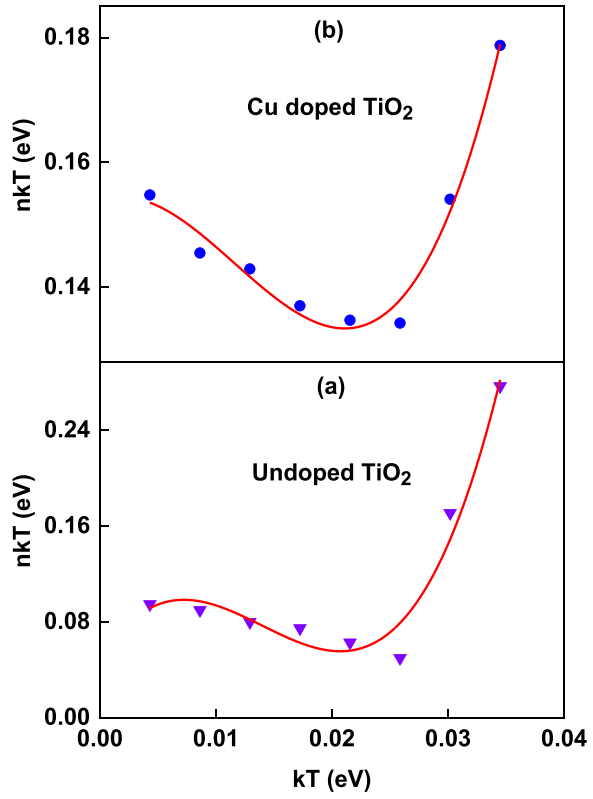

Fig. 4. The nkT versus kT plots of a) Al/TiO_2/n-Si and b) Al/Cu:TiO_2/n-Si devices.

is considered, the current in Eq. (1) is changed by the next form [41]:

$$I = I_0 \exp\left(\frac{q(V - IR_s)}{nkT}\right) \tag{5}$$

This IR_s causes the voltage drop for the device. Thus, the Cheung functions are given by the following formula:

$$\frac{dV}{d(lnI)} = IR_s + n\frac{kT}{q} \tag{6}$$

$$H(I) = V - n\left(\frac{kT}{q}\right) ln\left(\frac{I}{AA^*T^2}\right) \tag{7}$$

If Eq (7) are rearranged, the last version of the $H(I)$ are obtained by below relation:

$$H(I) = IR_s + n\Phi_b \tag{8}$$

If both the functions in Eqs. (6) and (8) are plotted against to current, the linear graphs are obtained in the ideal case. The slopes of these plots provide to determine the two R_s values of the device and show the consistency of Cheung method. While the intercept of the $dV/d(\ln I)$ versus I plots gives the n values, the intercept of the $H(I)$–I plots helps to find the $\Phi_b$values of the devices.

The $dV/d(\ln I)$-I and $H(I)$–I graphs of the Al/TiO_2/n-Si and Al/Cu:TiO_2/n-Si devices have been displayed in Fig. 6 and Fig. 7, respectively. The obtained n, $\Phi_b$and R_s values were listed in Tables 1 and 2 for the devices. Normally, $dV/d(\ln I)$-I and $H(I)$–I plots exhibits straight lines, but in this case, the non-ideal device structure and interfacial layers caused to deviate from the linearity. The n values obtained from Cheung method are in good harmony with the n values determined thermionic emission theory for the Al/TiO_2/n-Si device (averagely absolute errors for n is 0.43), but there are more differences between the n values for the Al/Cu:TiO_2/n-Si device at the same temperature (averagely absolute errors for n is 3.73). The differences at n values for two devices can be attributed to the Cu doping effect of the TiO_2 film layer. There are some differences at the $\Phi_b$values depending on the approximation differences between the two methods, but the differences are not big for both devices (averagely absolute errors for barrier heights have been shown under Tables 1 and 2) [42]. The determined R_s values from the $dV/d(\ln I)$-I and $H(I)$–I plots are close to each other and confirm the consistency of Cheung method.

Norde method provides to determine the Φ_b and R_s values as an alternative to Cheung method. According to this method, the Norde function is given via the following formula [43]:

$$F(V) = \frac{V}{\gamma} - \frac{kT}{q} ln\left(\frac{I(V)}{AA^*T^2}\right) \tag{9}$$

where γ represents dimensionless integer and greater than n. The $I(V)$ shows voltage dependent current value. The R_s and Φ_b values are extracted from the Norde function and given by the next equations:

$$\Phi_b = F(V_0) + \left[\frac{V_0}{\gamma} - \frac{kT}{q}\right] \tag{10}$$

$$R_s = \frac{\gamma - n}{I} \frac{kT}{q} \tag{11}$$

where $F(V_0)$ is the minimum point of $F(V)$ and V_0 is the corresponding voltage.

Fig. 8a and b indicate $F(v)$-V graphs of the Al/TiO_2/n-Si and Al/Cu:TiO_2/n-Si devices in the range of 50 K–400 K, respectively. The Φ_b and R_s values were calculated and listed in Tables 1 and 2 for the Al/TiO_2/n-Si and Al/Cu:TiO_2/n-Si devices from the $F(v)$-V graphs. The Φ_b

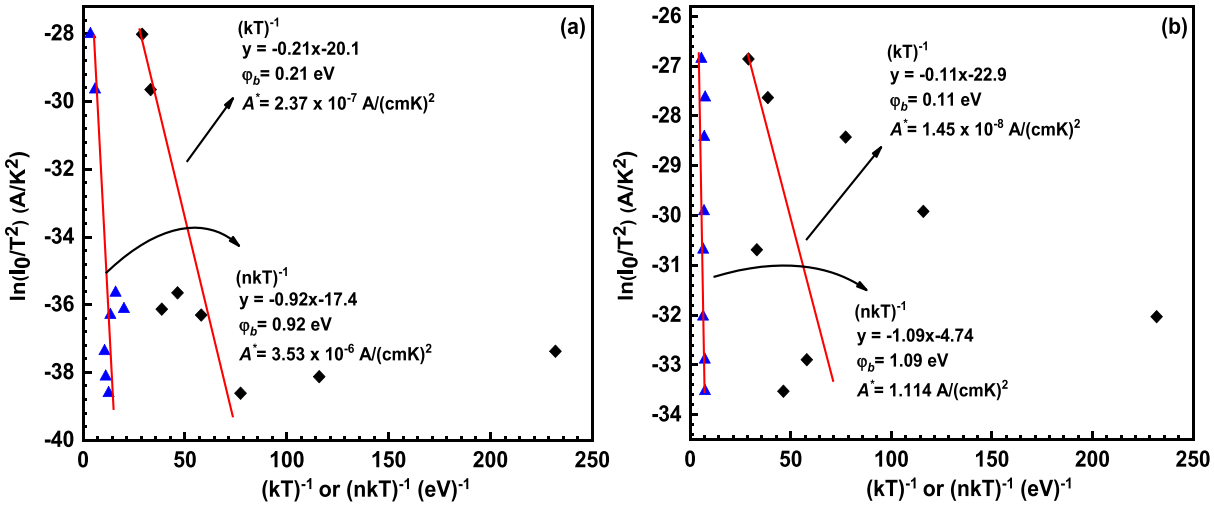

Fig. 5. The experimental Richardson plots a) Al/TiO_2/*n*-Si and b) Al/Cu:TiO_2/*n*-Si devices.

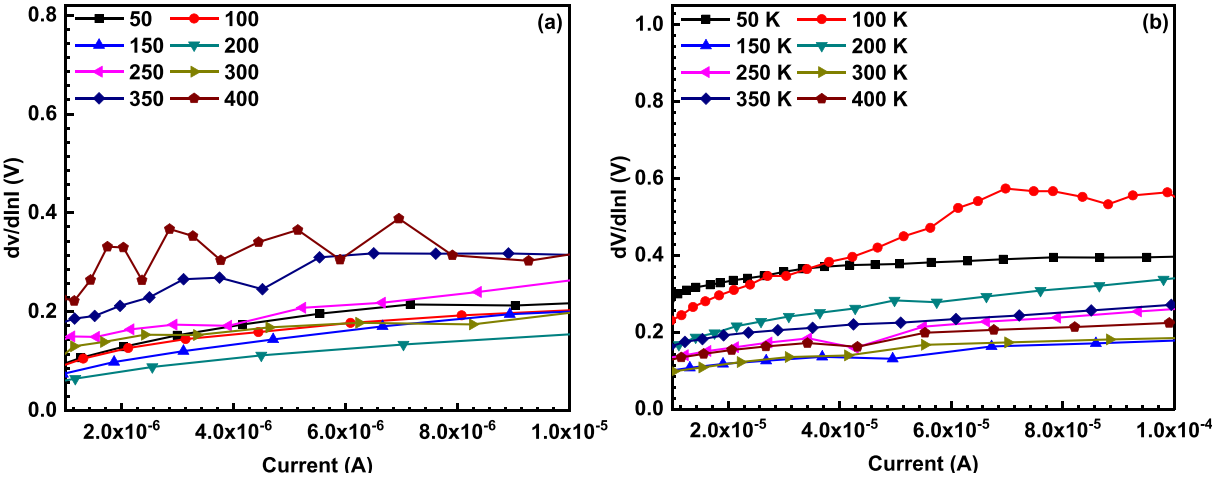

Fig. 6. *dv/dln(I)–I* plots of a) Al/TiO_2/*n*-Si and b) Al/Cu:TiO_2/*n*-Si devices for various temperatures.

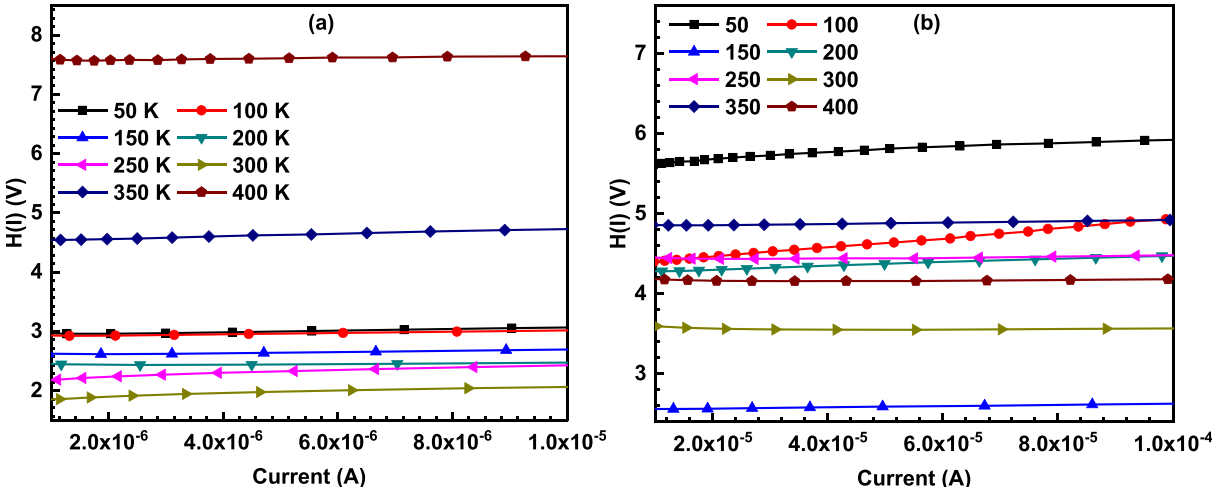

Fig. 7. *H(I)–I* plots of a) Al/TiO_2/*n*-Si and b) Al/Cu:TiO_2/*n*-Si devices for various temperatures.

values are in good agreement with the obtained Φ_b values from the thermionic emission theory. The R_s values are lower than that of R_s values from the Cheung method for both devices. The reason for different R_s values can be attributed to non-ideal device structure and approximation differences [44,45].

We studied temperature dependent profile of interface states density (N_{ss}) for the Al/TiO_2/*n*-Si and Al/Cu:TiO_2/*n*-Si devices. The N_{ss} values are obtained from the forward bias *I–V* measurements by considering efficient barrier height (Φ_e), ideality factor $n(V)$ and R_s. The Φ_e is given by the next formula [46]:

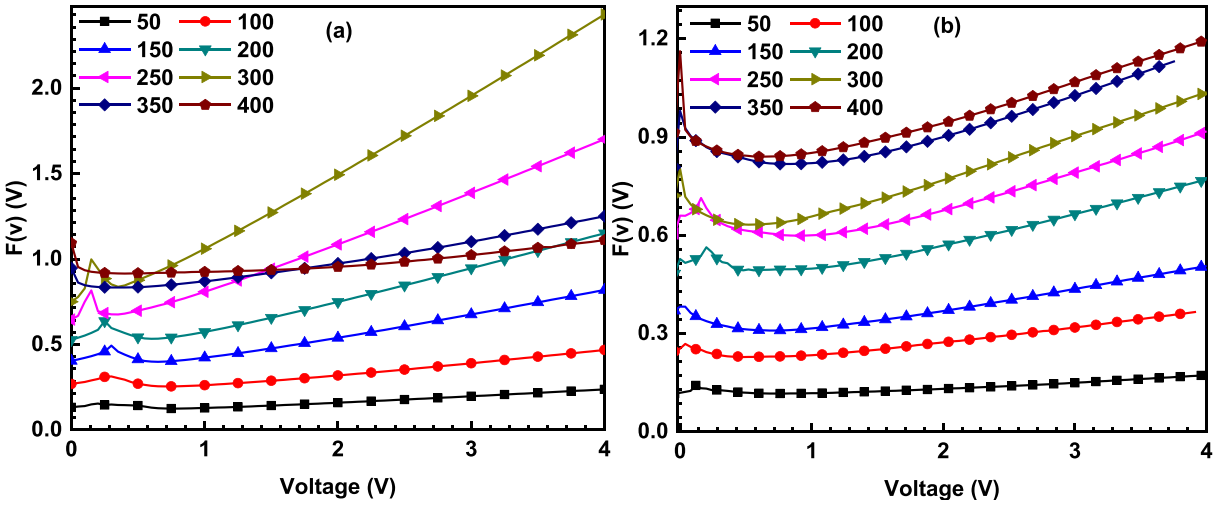

Fig. 8. *F(v)-V* graphs of a) Al/TiO_2/*n*-Si and b) Al/Cu:TiO_2/*n*-Si devices in the range of 50 K–400 K.

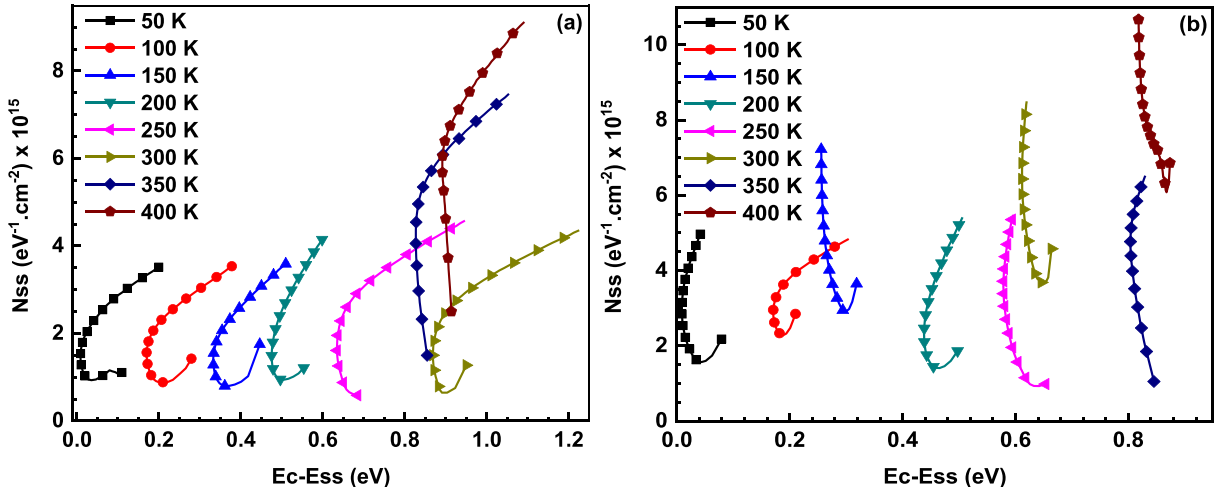

Fig. 9. N_{ss} versus $E_c - E_{ss}$ plots a) Al/TiO_2/*n*-Si and b) Al/Cu:TiO_2/*n*-Si devices for various temperatures.

$$\Phi_e = \Phi_b + (1 - 1/n(V))(V - IR_s) \tag{12}$$

The voltage dependent ideality factor values are calculated by the next equation according to Card and Rhoderick [47]:

$$n(V) = 1 + \frac{\delta}{\varepsilon_i}\left[\frac{\varepsilon_s}{W_d} + qN_{ss}(V)\right] \tag{13}$$

where δ is the thickness of the layer at the interface (200 nm in this case), ε_i is permittivity of the interfacial layer, W_d is depletion layer width, ε_s is permittivity of the semiconductor and N_{ss} exhibits interface state density. If equation (13) rearranged, the N_{ss} is obtained as the following formation:

$$N_{ss}(V) = \frac{1}{q}\left[\frac{\varepsilon_i}{\delta}(n(V) - 1) - \frac{\varepsilon_s}{W_d}\right] \tag{14}$$

If the N_{ss} is plotted to conduction band edge of the semiconductor from the semiconductor surface, the energy difference between conduction band edge and the surface should be calculated by the following equation:

$$E_C - E_{ss} = q(\Phi_e - (V - IR_s)) \tag{15}$$

The N_{ss} versus $E_c - E_{ss}$ plots of the Al/TiO_2/*n*-Si and Al/Cu:TiO_2/*n*-Si devices have been displayed for various temperatures in Fig. 9a and b, respectively. The N_{ss} values generally shifted to lower band edge with increasing temperature and reached higher values. Fig. 9 clearly exhibited that the N_{ss} values increased after Cu doping to the TiO_2 layer depending on the increasing defect in the interface. In addition, we can conclude that the N_{ss} values are a function of the temperature.

4. Conclusion

We obtained undoped and Cu doped TiO_2 thin films by spin coating technique and employed as an interfacial layer between the Al and *n*-Si to obtain Al/TiO_2/*n*-Si and Al/Cu:TiO_2/*n*-Si devices. We characterized the Al/TiO_2/*n*-Si and Al/Cu:TiO_2/*n*-Si devices for the temperature range of 50 K–400 K by the *I–V* measurements. The ln*I-V* measurements revealed that the currents of the devices are a strong function of the temperature, and the devices can be performed as a thermal detector at reverse biases. Furthermore, the current values of the Al/Cu:TiO_2/*n*-Si device are higher than the Al/TiO_2/*n*-Si device depending on the increasing carriers. The device parameters such as ideality factor, barrier height and series resistance were calculated by thermionic emission theory, Cheung and Norde method. The ideality factor values decreased with increasing temperature, the barrier height values increased. The temperature dependence at the barrier height and ideality factor exhibited barrier inhomogeneity in the interface of the devices. The series resistance values decreased with increasing temperature. The Al/Cu:TiO_2/*n*-Si device are lower series resistance than the Al/TiO_2/*n*-Si device. On the other hand, the current transport mechanism of the devices is not pure thermionic emission. The *nkT* versus *kT* plots

confirmed that the devices have thermionic field emission with the thermionic emission transport mechanism. The experimental Richardson plots approved that the devices have lower Richardson constant than the real value depending on barrier inhomogeneity. In addition, The N_{ss} versus E_{ss} - E_v plots of the Al/TiO_2/*n*-Si and Al/Cu:TiO_2/*n*-Si devices showed that N_{ss} values almost shifted to lower band edge values with increasing temperature. The results revealed that both the Al/TiO_2/*n*-Si and Al/Cu:TiO_2/*n*-Si devices can be employed in various applications in the wide range temperatures.

Acknowledgments

This work is supported by Selçuk University BAP office with Project Numbers 16401044. Authors would like to acknowledge the support of the Selçuk University for this research.

References

[1] P. Casey, G. Hughes, Photoemission study of the SiO2 conversion mechanism to magnesium silicate, J. Appl. Phys. 107 (2010) 074107, , https://doi.org/10.1063/1.3357392.
[2] S. Bhatia, N. Verma, R.K. Bedi, Varied sensing characteristics of in- doped ZnO films prepared by sol gel spin coating technique, Int. J. Pure Appl. Phys. 13 (2017) 973–1776 http://www.ripublication.com/ijpapspl/ijpapv13n1spl_10.pdf.
[3] J.S. Shaikh, N.S. Shaikh, S.S. Mali, J.V. Patil, K.K. Pawar, P. Kanjanaboos, C.K. Hong, J.H. Kim, P.S. Patil, Nanoarchitectures in dye-sensitized solar cells: metal oxides, oxide perovskites and carbon-based materials, Nanoscale 10 (2018) 4987–5034, https://doi.org/10.1039/C7NR08350E.
[4] M. Yilmaz, Ş. Aydoğan, The effect of Mn incorporation on the structural, morphological, optical, and electrical features of nanocrystalline ZnO thin films prepared by chemical spray pyrolysis technique, Metall. Mater. Trans. A 46 (2015) 2726–2735, https://doi.org/10.1007/s11661-015-2875-7.
[5] A. Kocyigit, D. Tatar, A. Battal, M. Ertugrul, B. Duzgun, M. Ertuğrul, A.B. Duzgun, Highly efficient optoelectronic properties of doubly doped SnO2 thin film deposited by spin coating technique, J. Ovonic Res. 8 (2012) 171–178.
[6] C.P. Liu, Y.Y. Hui, Z.H. Chen, J.G. Ren, Y. Zhou, L. Tang, Y.B. Tang, J.A. Zapien, S.P. Lau, Solution-processable graphene oxide as an insulator layer for metal–insulator–semiconductor silicon solar cells, RSC Adv. 3 (2013), https://doi.org/10.1039/c3ra42967a 17918.
[7] C.Y. Liu, H.Y. Xu, Y. Sun, J.G. Ma, Y.C. Liu, ZnO ultraviolet random laser diode on metal copper substrate, Opt. Express 22 (2014) 16731, https://doi.org/10.1364/OE.22.016731.
[8] M. Yıldırım, A. Kocyigit, Characterization of Al/In:ZnO/p-Si photodiodes for various in doped level to ZnO interfacial layers, J. Alloy. Comp. (2018), https://doi.org/10.1016/j.jallcom.2018.07.295.
[9] I. Orak, M. Toprak, A. Turut, Illumination impact on the electrical characterizations of an Al/Azure A/p-Si heterojunction, Phys. Scr. 89 (2014), https://doi.org/10.1088/0031-8949/89/11/115810 115810.
[10] A. Kocyigit, İ. Karteri, I. Orak, S. Uruş, M. Çaylar, The structural and electrical characterization of Al/GO-SiO2/p-Si photodiode, Phys. E Low-Dimensional Syst. Nanostructures. 103 (2018) 452–458, https://doi.org/10.1016/j.physe.2018.06.006.
[11] Y. Şafak-Asar, T.T. Asar, Ş. Altındal, S. Özçelik, Ş. Altindal, S. Özçelik, Investigation of dielectric relaxation and ac electrical conductivity using impedance spectroscopy method in (AuZn)/TiO2/p-GaAs(1 1 0) Schottky barrier diodes, J. Alloy. Comp. 628 (2015) 442–449, https://doi.org/10.1016/j.jallcom.2014.12.170.
[12] A. Kumar, S. Mondal, S.G. Kumar, K.S.R. Koteswara Rao, High performance sol–gel spin-coated titanium dioxide dielectric based MOS structures, Mater. Sci. Semicond. Process. 40 (2015) 77–83, https://doi.org/10.1016/j.mssp.2015.06.073.
[13] Y. Şafak Asar, T. Asar, Ş. Altındal, S. Özçelik, Dielectric spectroscopy studies and ac electrical conductivity on (AuZn)/TiO 2/p-GaAs(110) MIS structures, Philos. Mag. 95 (2015) 2885–2898, https://doi.org/10.1080/14786435.2015.1081301.
[14] W. Jin, K. Zhang, Z. Gao, Y. Li, L. Yao, Y. Wang, L. Dai, CdSe nanowire-based flexible devices: Schottky diodes, metal–semiconductor field-effect transistors, and inverters, ACS Appl. Mater. Interfaces 7 (2015) 13131–13136, https://doi.org/10.1021/acsami.5b02929.
[15] A. Shetty, B. Roul, S. Mukundan, L. Mohan, G. Chandan, K.J. Vinoy, S.B. Krupanidhi, Temperature dependent electrical characterisation of Pt/HfO2/n-GaN metal-insulator-semiconductor (MIS) Schottky diodes, AIP Adv. 5 (2015) 097103, , https://doi.org/10.1063/1.4930199.
[16] A. Kocyigit, I. Orak, İ. Karteri, S. Uruş, The structural analysis of MWCNT-SiO2 and electrical properties on device application, Curr. Appl. Phys. 17 (2017) 1215–1222, https://doi.org/10.1016/j.cap.2017.05.006.
[17] M. Gökçen, H. Altuntaş, Ş. Altındal, S. Özçelik, Frequency and voltage dependence of negative capacitance in Au/SiO2/n-GaAs structures, Mater. Sci. Semicond. Process. 15 (2012) 41–46, https://doi.org/10.1016/j.mssp.2011.08.001.
[18] S. Kaya, E. Yilmaz, A comprehensive study on the frequency-dependent electrical characteristics of Sm2O3 MOS capacitors, IEEE Trans. Electron Devices 62 (2015) 980–987, https://doi.org/10.1109/TED.2015.2389953.
[19] Y. Badali, Ş. Altındal, İ. Uslu, Dielectric properties, electrical modulus and current transport mechanisms of Au/ZnO/n-Si structures, Prog. Nat. Sci. Mater. Int. 28 (2018) 325–331, https://doi.org/10.1016/J.PNSC.2018.05.003.
[20] E.E. Tanrıkulu, D.E. Yıldız, A. Günen, Ş. Altındal, Frequency and voltage dependence of electric and dielectric properties of Au/TiO 2/n-4H-SiC (metal-insulator-semiconductor) type Schottky barrier diodes, Phys. Scr. 90 (2015) 095801, , https://doi.org/10.1088/0031-8949/90/9/095801.
[21] A.K. Bilgili, T. Güzel, M. Özer, Current-voltage characteristics of Ag/TiO2/n-InP/Au Schottky barrier diodes, J. Appl. Phys. 125 (2019) 035704, , https://doi.org/10.1063/1.5064637.
[22] A. Tataroğlu, A.G. Al-Sehemi, M. Ilhan, A.A. Al-Ghamdi, F. Yakuphanoglu, Optical, electrical and photoresponse properties of Si-based diodes with NiO-doped TiO2 film prepared by sol-gel method, Siliconindia 10 (2018) 913–920, https://doi.org/10.1007/s12633-016-9548-z.
[23] M. Yıldırım, Characterization of the framework of Cu doped TiO2 layers: an insight into optical, electrical and photodiode parameters, J. Alloy. Comp. 773 (2019) 890–904, https://doi.org/10.1016/J.JALLCOM.2018.09.276.
[24] F. Bensouici, M. Bououdina, A.A. Dakhel, M. Tounane, A. Iratni, T. Souier, S. Liu, W. Cai, Optical, structural and photocatalysis properties of Cu-doped TiO2 thin films, Appl. Surf. Sci. 35 (2017) 110–116, https://doi.org/10.1016/j.apsusc.2016.07.034.
[25] Q. Wang, J. Qiao, X. Xu, S. Gao, Controlled synthesis of Cu nanoparticles on TiO2 nanotube array photoelectrodes and their photoelectrochemical properties, Mater. Lett. 131 (2014) 135–137, https://doi.org/10.1016/j.matlet.2014.05.086.
[26] G. Blondeau, M. Froelicher, M. Froment, A. Hugot-Le Goff, J. Zerbino, Influence of copper addition on optical properties of TiO2, J. Electrochem. Soc. 126 (1979) 1592–1596, https://doi.org/10.1149/1.2129337.
[27] D. Dhruv, Z. Joshi, S. Kansara, D.D. Pandya, J.H. Markna, K. Asokan, P.S. Solanki, D.G. Kuberkar, N.A. Shah, Temperature-dependent I–V and C–V characteristics of chemically-grown Y0.95Ca0.05MnO3/Si thin films, Mater. Res. Express 3 (2016) 036402, , https://doi.org/10.1088/2053-1591/3/3/036402.
[28] E. Marıl, A. Kaya, H.G. Çetinkaya, S. Koçyiğit, Ş. Altındal, On the temperature dependent forward bias current–voltage (I–V) characteristics in Au/2% graphene–cobalt doped (Ca3Co4Ga0.001Ox)/n-Si structure, Mater. Sci. Semicond. Process. 39 (2015) 332–338, https://doi.org/10.1016/j.mssp.2015.05.029.
[29] İ. Taşçıoğlu, S.O. Tan, F. Yakuphanoğlu, Ş. Altındal, Effectuality of barrier height inhomogeneity on the current–voltage–temperature characteristics of metal semiconductor structures with CdZnO interlayer, J. Electron. Mater. 47 (2018) 6059–6066, https://doi.org/10.1007/s11664-018-6495-z.
[30] G. Perez, G. Chicot, Y. Avenas, P. Lefranc, P.O. Jeannin, D. Eon, N. Rouger, Integrated temperature sensor with diamond Schottky diodes using a thermosensitive parameter, Diam. Relat. Mater. 78 (2017) 83–87, https://doi.org/10.1016/j.diamond.2017.08.008.
[31] I. Jyothi, V. Janardhanam, H. Hong, C.-J. Choi, Current–voltage and capacitance–voltage characteristics of Al Schottky contacts to strained Si-on-insulator in the wide temperature range, Mater. Sci. Semicond. Process. 39 (2015) 390–399, https://doi.org/10.1016/j.mssp.2015.05.043.
[32] M. Ali Yildirim, B. Güzeldir, A. Ate, M. Salam, Temperature dependent current-voltage characteristics of the Zn/ZnO/n-Si/Au-Sb structure with ZnO interface layer grown on n-Si substrate by SILAR method, Microelectron. Eng. 88 (2011) 3075–3079, https://doi.org/10.1016/j.mee.2011.05.025.
[33] D.S. Reddy, M.S.P. Reddy, V.R. Reddy, Analysis of current-voltage-temperature (I-V-T) and of Pt/Ti Schottky contacts, on n-type InP 5 (2011) 448–454.
[34] S. Kumar, Y.S. Katharria, S. Kumar, D. Kanjilal, Temperature-dependent barrier characteristics of swift heavy ion irradiated Au/n-Si Schottky structure, J. Appl. Phys. 100 (2006), https://doi.org/10.1063/1.2388855 113723.
[35] F.E. Cimilli, H. Efeoğlu, M. Sağlam, A. Türüt, Temperature-dependent current–voltage and capacitance–voltage characteristics of the Ag/n-InP/In Schottky diodes, J. Mater. Sci. Mater. Electron. 20 (2009) 105–112, https://doi.org/10.1007/s10854-008-9635-z.
[36] A. Guzel, S. Duman, N. Yildirim, A. Turut, Electronic transport of an Ni/n-GaAs diode analysed over a wide temperature range, J. Electron. Mater. 45 (2016) 2808–2814, https://doi.org/10.1007/s11664-016-4342-7.
[37] K. Ejderha, N. Yıldırım, B. Abay, A. Turut, Examination by interfacial layer and inhomogeneous barrier height model of temperature-dependent I–V characteristics in Co/p-InP contacts, J. Alloy. Comp. 484 (2009) 870–876, https://doi.org/10.1016/J.JALLCOM.2009.05.062.
[38] N. Shiwakoti, A. Bobby, K. Asokan, B. Antony, Temperature dependent dielectric studies of Ni/n-GaP Schottky diodes by capacitance and conductance measurements, Mater. Sci. Semicond. Process. 42 (2016) 378–382, https://doi.org/10.1016/j.mssp.2015.11.010.
[39] M.A. Mayimele, J.P.J. Van Rensburg, F.D. Auret, M. Diale, Analysis of temperature-dependant current-voltage characteristics and extraction of series resistance in Pd/ZnO Schottky barrier diodes, Phys. B Condens. Matter 480 (2016) 58–62, https://doi.org/10.1016/j.physb.2015.07.034.
[40] M. Özer, D.E. Yıldız, Ş. Altındal, M.M. Bülbül, Temperature dependence of characteristic parameters of the Au/SnO2/n-Si (MIS) Schottky diodes, Solid State Electron. 51 (2007) 941–949, https://doi.org/10.1016/J.SSE.2007.04.013.
[41] S.K. Cheung, N.W. Cheung, Extraction of Schottky diode parameters from forward current-voltage characteristics, Appl. Phys. Lett. 49 (1986), https://doi.org/10.1063/1.97359 85.
[42] Ş. Karataş, Effect of series resistance on the electrical characteristics and interface state energy distributions of Sn/p-Si (MS) Schottky diodes, Microelectron. Eng. 87 (2010) 1935–1940, https://doi.org/10.1016/j.mee.2009.11.168.
[43] H. Norde, A modified forward I-V plot for Schottky diodes with high series resistance, J. Appl. Phys. 50 (1979) 5052–5053, https://doi.org/10.1063/1.325607.
[44] Ş. Karataş, N. Yildirim, A. Türüt, Electrical properties and interface state energy

distributions of Cr/n-Si Schottky barrier diode, Superlattice Microstruct. 64 (2013) 483–494, https://doi.org/10.1016/j.spmi.2013.10.015.
[45] O.S. Cifci, A. Kocyigit, P. Sun, Perovskite/p-Si photodiode with ultra-thin metal cathode, Superlattice Microstruct. 120 (2018) 492–500, https://doi.org/10.1016/J.SPMI.2018.06.009.
[46] Ç. Bilkan, A. Gümüş, Ş. Altındal, The source of negative capacitance and anomalous peak in the forward bias capacitance-voltage in Cr/p-si Schottky barrier diodes (SBDs), Mater. Sci. Semicond. Process. 39 (2015) 484–491, https://doi.org/10.1016/j.mssp.2015.05.044.
[47] H.C. Card, E.H. Rhoderick, Studies of tunnel MOS diodes I. Interface effects in silicon Schottky diodes, J. Phys. D Appl. Phys. 4 (1971), https://doi.org/10.1088/0022-3727/4/10/319 319.